

A novel solar-driven Organic Rankine Cycle system based on the two-stage solar thermal collection and accumulation

Datong Gao ^{a,b}, Jing Li ^{c,*}, Yong Hao ^{d,e}, Gang Pei ^{a,b*}

^a *Department of Thermal Science and Energy Engineering, University of Science and Technology of China, Hefei 230027, China*

^b *Key Laboratory of Solar Thermal Conversion of Anhui Province, Hefei 230027, China*

^c *Research Center for Sustainable Energy Technologies, Energy and Environment Institute, University of Hull, Hull, UK*

^d *Institute of Engineering Thermophysics, Chinese Academy of Sciences, Beijing 100190, China*

^e *University of Chinese Academy of Sciences, Beijing 100049, China*

Abstract

Solar thermal power has attracted much attention because it is instrumental to solar energy storage and power grid peak shaving. Among the various solar thermal power technologies, the Organic Rankine Cycle stands out as a prevalent choice for low and intermediate-temperature (80 – 200 °C) solar thermal power generation applications. However, it is required of the concentrating solar collectors for medium temperature supply and its performance is greatly affected by the off-design operation owing to variable solar irradiance. In this paper, a novel solar-driven Organic Rankine Cycle system that consists of a two-stage solar thermal collection and accumulation design is proposed to solve the above issues. Two-stage non-concentrating solar plants are adopted to harvest global solar irradiance and regulate system operation. Two-stage energy accumulators can not only mitigate the influence of the solar irradiance

* Corresponding authors.

E-mail addresses: lijing83@ustc.edu.cn (J. Li), peigang@ustc.edu.cn (G. Pei).

fluctuation on the Organic Rankine Cycle off-design running but also enhance the temperature drop of thermal energy storage. Through the experimental test and numerical simulation, the results indicate that the influence of solar irradiance on the Organic Rankine Cycle steady operation has been weakened (reducing power output fluctuation range by approximately 70%), and the overall system efficiency has also been improved by 43.85%. Consequently, the solar Organic Rankine Cycle system proposed in this paper exhibits superior thermal performance compared to the conventional systems and is conducive to the advancement of the non-concentrating solar thermal power system.

Keywords: Solar energy; Organic Rankine Cycle; Renewable energy system.

Nomenclature

Symbol

A	area, m^2
b	the average width of the welding material, m
c_p	specific heat capacity, $J/(kg \cdot K)$
D	diameter of the tube, m
E	enhancement factor
f	the average thickness of the welding material, m
g	gravitational acceleration, m/s^2
G	mass flux, $kg/(m^2 \cdot s)$
h	heat transfer coefficient, $W/(m^2 \cdot K)$
H	enthalpy, J
I	solar irradiance, W/m^2
l	length, m
m	mass flow rate, kg/s
M	molecular mass, g/mol

p	Pressure, Pa
p_r	pressure ratio
q	thermal flux, W/m ²
r	phase change latent heat, J/kg
R	pressure drop factor
S	suppression factor
T	temperature, K
T_i^*	normalized temperature difference, K•m ² /W
v	velocity, m/s
V	volume, m ³
w	power, W
x	vapor quality

Abbreviation

Bo	boiling number
EFPC	evacuated flat-plate solar collector
HTA	high-temperature accumulator
HTF	heat transfer fluid
LTA	low-temperature accumulator
MRE	mean relative error
ORC	Organic Rankine Cycle
Pr	Prandtl number
Re	Renold number
Xtt	Martinelli number

Subscripts

2p	two phases
a	ambient
abs	absorber plate
b	back plate
c	convection

cond	conductivity
eva	evaporator
exp	experiment
f	fluid
g	vapor phase
gen	generator
gla	glass
grd	ground
in	inlet
l	liquid phase
nb	nucleate boiling
out	outlet
p	pump
r	radiation
s	isentropic
SF	solar field
sim	simulation
tb	absorber tube
tur	turbine

Greek letter

α	absorptance
γ	surface tension, N/m
ε	emittance
η	efficiency
λ	thermal conductivity, W/(m•K)
μ	dynamic viscosity, Pa•s
ρ	density, kg/m ³
σ	Stefan-Boltzmann constant, 5.67×10^8 W/(m ² •K ⁴)
τ	transmittance

1. Introduction

Amidst the goal of achieving carbon neutrality, the promotion of renewable energy penetration in the residential and industrial sectors has garnered significant attention [1]. As one of the cleanest renewable energy types, solar energy can be widely used for the provision of various energy forms, such as electricity and thermal energy [2]. Although solar photovoltaic technology has been extensively adopted globally for its competitive price and convenient installation [3], its output capacity is greatly dependent on solar irradiation magnitude [4], often resulting in relatively higher electrical energy storage costs [5]. Solar thermal power technology is capable of solving the above issue owing to its low energy storage cost and peak load regulation capacity [6]. Additionally, in light of the life cycle assessment of solar photovoltaic and solar thermal panels, the latter proves to be more environmentally friendly and easy to recycle [7]. Over the last decade, the worldwide installed solar thermal power capacity increased from 1106.3 MW in 2010 to 6596.6 MW in 2020, experiencing a compound annual growth rate of 19.5%. It is anticipated that the global installed solar thermal power capacity will reach 14172.8 MW by 2030 [8]. Presently, solar thermal power technology plays an increasingly prominent role in regulating the installed capacity of intermittent renewable energy (wind power, solar photovoltaic, etc.), thereby facilitating the transition towards a robust power grid operating predominantly on renewable energy and ensuring its safe and stable operation.

Current research in solar thermal power primarily focuses on the utilization of concentrating solar collectors, such as parabolic trough solar collectors [9], and solar

tower solar collectors [10]. These collectors have the advantage of serving as a higher temperature source, thus increasing the efficiency of the subsequent thermodynamic cycle (such as the steam Rankine cycle [11] or CO₂ Brayton cycle [12]). However, the shortcoming of concentrating solar collectors lies in that they need a highly accurate tracking device to cooperate with the solar harvesting process, and only beam solar irradiance can be utilized [13]. This restricts their widespread application in regions with dense populations where full utilization of the available solar resource may not be feasible. For the non-concentrating solar collector (such as flat-plate solar collector [14] and evacuated tube solar collector [15]), the solar-driven ORC system [16] is preferred for electricity generation because of its low evaporation temperature requirement [17].

The efficiency of the solar-driven ORC system is influenced by both the solar harvesting process and the ORC running characteristics. For solar thermal collection, the thermal loss will increase tremendously with increasing operating temperature [18] despite the concentrating or non-concentrating solar collectors. Therefore, the research on the reduction of thermal loss during solar harvesting aroused wide attention. Various approaches have been studied, including the aerogel transparent thermal insulation structure [19, 20], the nanofluid for energy transportation enhancement [15, 21], and the thermal loss recycle design [22, 23], etc. The above research provides new pathways to solving the collector thermal loss problem. In terms of the ORC unit, the variable heat source temperature provided by the solar collector thus caused the off-design operation (performance degradation on the expander, pump, motor, and so on) will greatly impair the cycle efficiency [24]. Chatzopoulou et al. [25] have proposed an off-

design optimization method to predict the impact of varying heat-source conditions on ORC operation. Hu et al. [26] investigated the impact of varying evaporation temperatures on an ORC unit that used an axial turbine, and they proposed alternative control strategies for the expander, thereby realizing the maximum performance during off-design operation. Maximilian Weitzer et al. [27] employed volumetric machines for two-phase expansion processes which mitigated the impact of off-design conditions (partial evaporation and flash evaporation) in Carnot batteries based on ORC. Therefore, the performance improvement of solar-driven ORC systems should be comprehensively considered both in the energy collection and storage process.

The inherent property of solar energy leads to a continuously changing solar irradiance magnitude throughout the day [28]. Given the above characteristics of the solar-driven ORC system, its thermal power generation performance highly relies on the ambient conditions, potentially resulting in the off-design condition of the ORC unit and electricity generation fluctuating with the solar irradiance magnitude. Such unstable solar thermal power output can be detrimental to both the power grid and users. [29]. To tackle this problem, thermal energy storage devices are extensively deployed in solar thermal power plants, such as molten salts [30] and water tanks [31].

However, thermal energy storage technology is also confronted with the following challenges in its implementation. On the one hand, the economic benefits of traditional thermal energy storage are primarily applicable to large-scale solar plants (exceeding MW level) [32]. With the development of solar-driven ORC district energy systems [33], relatively small-scale thermal energy storage will lead to a non-negligible energy

loss and high investment costs [34]. On the other hand, the evaporation temperature requirement of the ORC unit imposes limitations on the temperature drop range of the heat storage device. This constraint ensures the proper functioning of the ORC unit but may lead to limited energy storage capacity for these devices [35]. Moreover, the limited temperature drop range of the storage device causes a much higher average operating temperature of the solar field, thereby impairing the efficiency of solar thermal collection [36].

To overcome the above drawbacks of conventional non-concentrating solar ORC systems, a novel two-stage solar energy collection and accumulation ORC system is proposed. Its main design principle and advantages can be summarized as follows. Firstly, it adopts a two-stage evacuated flat-plate solar collector field which can work at both the direct steam generation and pressurized water mode, achieving a considerable thermal efficiency in the low and intermediate temperature range. Then, the system is designed with two-stage energy accumulators that can enable different working modes together with the two-stage solar field, which brings the whole system resistance capacity for the boundary conditions fluctuation. Therefore, the two-stage solar thermal collection and accumulation system proposed in this paper is expected to overcome the adverse impact of varying solar irradiance and provide a more considerable thermal energy storage capacity, thereby improving the overall system efficiency of the non-concentrating solar ORC system.

In recent studies that concern the solar ORC system optimization. Various system configurations have been proposed that focus on the cascade thermodynamic cycle, the

two-stage heat source, or the two-phase water/steam storage. For instance, Gao et al. [37] developed a cascade solar-driven ORC system with a two-stage water/steam storage method. Their novel two-stage storage and two-stage thermodynamic cycle have reached a high efficiency and cost-effective performance. Wang et al. [38] constructed a two-stage series evaporation ORC system with dual-level heat sources. Surendran et al. [39] investigated a dual waste heat source ORC system to increase its power output and reduce the heat exchanger requirement. The above similar system designs have shown the advantages of two-stage configuration. However, very few studies have simultaneously considered both solar thermal collection and storage with a two-stage configuration. Furthermore, the high-efficient non-concentrating solar collector applied for ORC system optimization also lack investigation.

The structure of this paper is organized as follows. The system configuration and operating strategy are elaborately described in Section 2. The numerical models of the components used in this system are established and validated by the experimental results in Section 3. In Section 4, the performance of this system and a comparison with the conventional single-stage solar-driven ORC system are elaborately presented. Finally, the main conclusions of this study are given in Section 5.

2. System Description

2.1 System configuration

The two-stage system configuration, as depicted in Fig. 1, comprises the solar plant, thermal energy accumulator, and ORC unit. The solar plant is designed with two stages: the first stage elevates the HTF (heat transfer fluid) temperature to the saturated

state, while the second stage is used to further heat the HTF to the two-phase state. A structure-optimized evacuated flat-plate solar collector is adopted in this study for solar thermal collection. It uses an internal vacuum environment to inhibit heat conduction and convection. Previous research has demonstrated that this novel solar collector can work in both the pressurized water mode and the direct steam generation mode [40] under non-concentrating solar irradiance. Thus, low-pressure steam can be obtained as the heat source for the ORC unit. With the two-phase flow in the solar field, the average operation temperature will be decreased, and the system working mode can be flexibly adjusted in light of the actual solar irradiance magnitude. At the same time, global solar irradiance is harvested with considerable efficiency under the intermediate temperature range (100 – 200 °C). Therefore, this novel solar collector is qualified for two-stage design construction undertaken in this study.

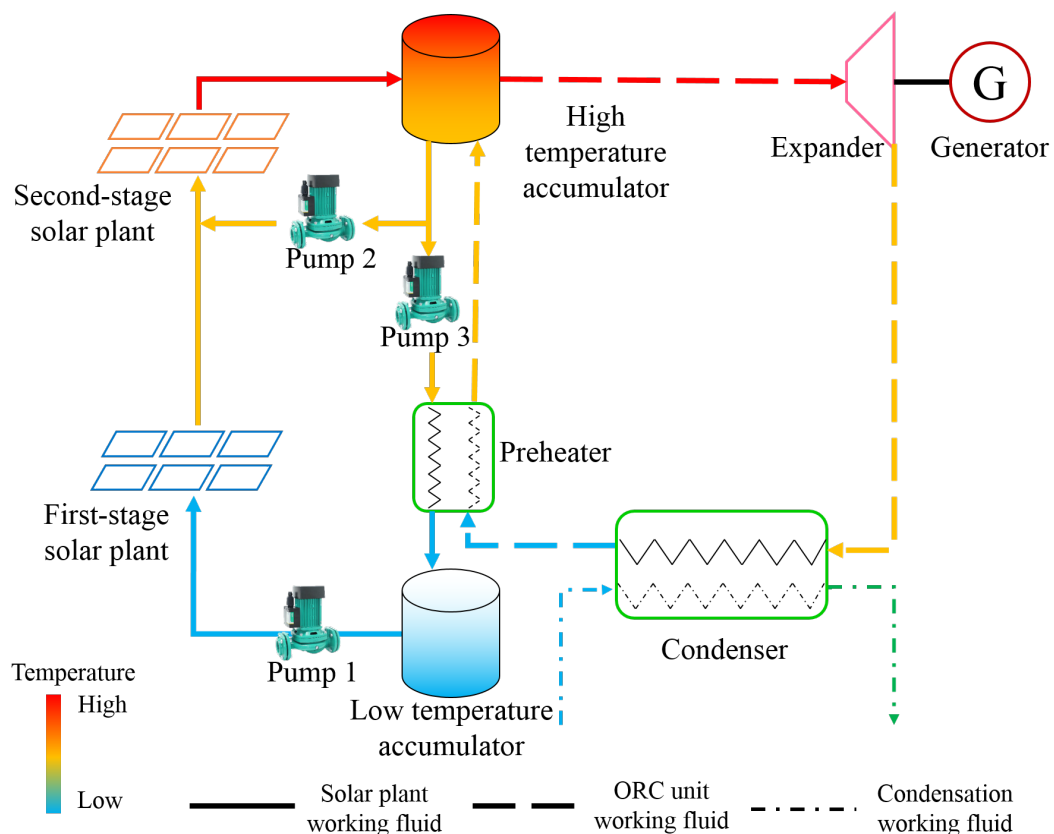


Fig. 1 Schematic of the two-stage solar thermal collection and accumulation ORC system.

Then, two-stage accumulators are employed to mitigate the impact of fluctuating solar irradiance on the evaporation temperature of the ORC unit and enhance the heat storage capacity of the thermal energy storage device, thereby realizing a more flexible system regulation. The first stage is an LTA (low-temperature accumulator) that is used to store the low-temperature HTF, while the second stage is an HTA (high-temperature accumulator) that is used to store the two-phase water/steam from the solar field and evaporating organic fluid for the ORC unit. The two-stage accumulator configuration can enlarge the temperature drop of thermal storage, providing benefits to both the solar field and ORC unit.

Additionally, a preheater is set between the solar field and the ORC unit avoids temperature fluctuation in the high-temperature accumulator. It can facilitate sufficient heat exchange with the solar field and avert large exergy losses in the HTF. Hence, the solar field can make a sufficient heat exchange with the ORC unit, leading to a substantial increase in large thermal storage capacity and overall system efficiency. The bypass channel from the HTA to the second-stage solar field is used to alleviate the strong solar fluctuation by adjusting the flow rate from both the LTA and HTA.

Furthermore, another advantage of the water/steam storage accumulator lies in its short relaxation time. Several studies have demonstrated that this two-phase heat storage medium has a quick evaporation and condensation rate [41], which brings great benefits to handling unpredictable solar irradiation conditions. Therefore, the water/steam working fluid pairs can benefit both solar thermal collection and energy

storage processes.

2.2 Operating strategy

Considering the diurnal time scale, the solar irradiance magnitude varies over time. To mitigate the effects of solar fluctuation and guarantee that the ORC unit runs steadily in its design situation, the operating strategy during a typical day is devised as follows.

Mode I: In the early morning, since the solar irradiance is weak, the flow rate from HTA is 0 (Pump 2 will be idle). By adjusting the flow rate from LTA to HTA (via Pump 1), the saturated state of the HTF at the second-stage solar field outlet is guaranteed. Under this circumstance, only the solar thermal collection process is running in this system, while the ORC unit will not work. The saturated state HTF will continuously increase in HTA under this working mode.

Mode II: At noon, the first-stage solar field is used to heat the heat transfer fluid (HTF) to the saturated state under the design operation temperature, while the second-stage solar field is used to further heat the HTF to the two-phase state. Since the solar irradiance is strong, the flow rate from HTA and LTA (via Pump 2) is adjusted synergistically to obtain a high steam quality from the second-stage solar field and avoid the superheated steam condition. The solar thermal collection and electricity generation from the ORC are in process simultaneously.

Mode III: At dusk and night, since the solar irradiance is very weak, the solar thermal collection process is halted. The HTF flows from the HTA to the LTA (via Pump 3) until depletion and thermal energy is utilized to drive the ORC unit for electricity generation.

3. Methodology

3.1 Solar field

The first-stage solar field uses pressurized water as the working fluid, and an experimental platform was constructed to prove its actual performance. As illustrated in Fig. 2, a medium-scale (50.96 m²) solar plant was constructed on the campus of the University of Science and Technology of China. This solar test platform adopted the evacuated flat-plate solar collector that possesses a structure-optimized design: it utilizes the internal vacuum environment to hinder thermal conduction and convection. This novel merit results in a considerable thermal efficiency in the intermediate temperature range (100 – 200 °C) that corresponds to the ORC unit operation. Furthermore, the efficiency curve and its fitting formula are also presented in Fig. 2. The related details about these studies (including the experimental process, measurement apparatus, etc.) can be found in [42]. Detailed main parameters are summarized in Table 1.

Table 1 The main parameters of the first-stage solar plant.

Term	Value
Absorber plate material	Al-based selective coating
Heat pipe material	Cu
HTF	Water and propylene glycol mixture at a 3:1 ratio
Absorptivity (solar band)	0.95
Emissivity (infrared band)	0.05
Heat absorption plate dimension (mm)	922×1952 (1.80 m ²)
Back plate material	AISI 441 stainless steel
Slope (°)	25
Max. Operating Pressure (MPa)	1.60

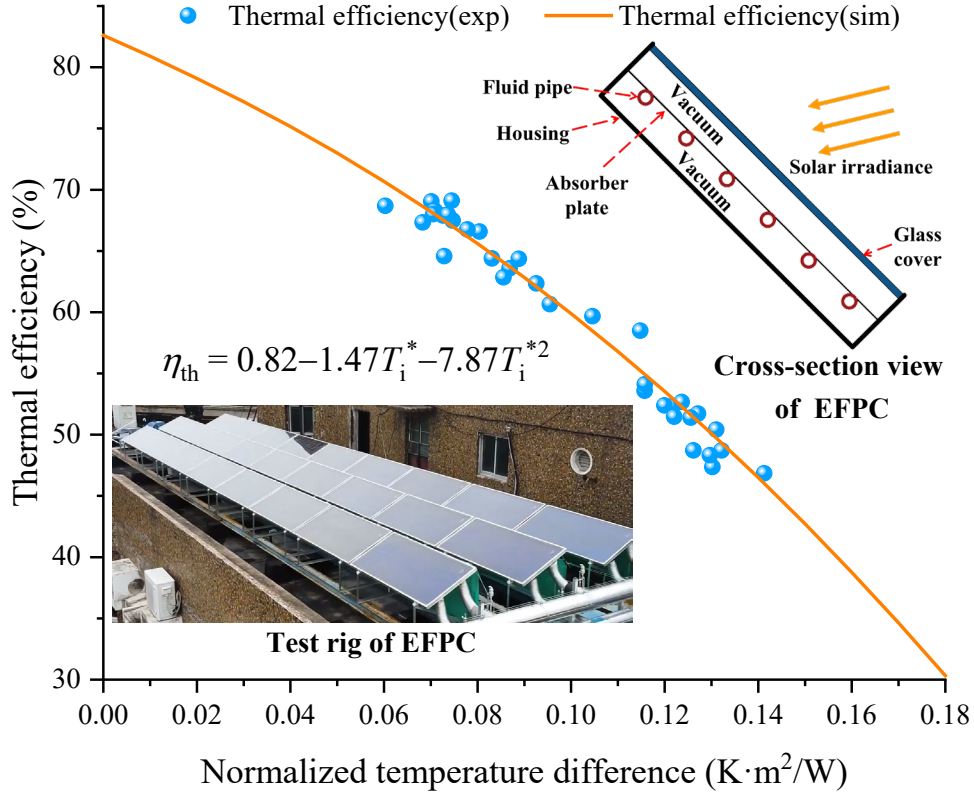


Fig. 2 The experimental and numerical results of the first-stage solar field.

In addition, the uncertainty of the experiment is also examined by the following uncertainty calculation model which is given by [43]:

$$\Delta\eta_{th} = \frac{\Delta q}{I} + \frac{q\Delta I}{I^2} \quad (1)$$

where,

$$\Delta q = c_p \left[\frac{\Delta m(T_o - T_i) + 2m\Delta T}{A_{abs}} \right] \quad (2)$$

The temperature sensor PT-100 is positioned at the inlet and outlet of the solar collector array, and its measuring precision is 0.1 °C; A Coriolis flowmeter with a measuring accuracy of 0.1 kg/h to measure the total mass flow rate of the solar field; and the pyranometer's precision is 0.1 W/m² for the global solar irradiance. According to the uncertainty analysis, the average uncertainty of the thermal efficiency during the

test time was 2.64%. Therefore, the measuring instruments can ensure the experimental results are highly accurate.

At the same time, a numerical model for the pressurized water running mode EFPC is established to access its thermal performance. For this model, the energy equilibrium equations for the key components (glass cover, absorber plate, etc.) in the solar collector are formulated, thereby deducing the thermal performance of the solar collector by the first law of thermodynamics.

The thermal equilibrium equation for the glass cover is [44]:

$$\alpha_{\text{gla}} I + h_{\text{r,abs-gla}} (T_{\text{abs}} - T_{\text{gla}}) = h_{\text{r,g-a}} (T_{\text{gla}} - T_{\text{a}}) + h_{\text{c,g-a}} (T_{\text{gla}} - T_{\text{a}}) \quad (3)$$

with,

$$h_{\text{r,abs-gla}} = \frac{\sigma(T_{\text{abs}}^2 + T_{\text{gla}}^2)(T_{\text{abs}} + T_{\text{gla}})}{\frac{1}{\varepsilon_{\text{abs}}} + \frac{1}{\varepsilon_{\text{gla}}} - 1} \quad (4)$$

$$h_{\text{r,gla-a}} = \frac{\varepsilon_{\text{gla}} \sigma (T_{\text{gla}}^4 - T_{\text{sky}}^4)}{(T_{\text{gla}} - T_{\text{a}})} \quad (5)$$

$$T_{\text{sky}} = 0.0552 T_{\text{a}}^{1.5} \quad (6)$$

$$h_{\text{c,gla-a}} = 5.7 + 3.8 v_{\text{wind}} \quad (7)$$

where, α_{gla} and ε_{gla} are the absorptivity and emissivity of the glass cover, respectively; ε_{abs} is the emissivity of the absorber plate; σ is the Stefan-Boltzmann constant, 5.67×10^8 W/(m²•K⁴); $h_{\text{r,abs-gla}}$ is the radiant heat transfer coefficient between the glass cover and absorber plate; $h_{\text{r,gla-a}}$ and $h_{\text{c,gla-a}}$ are the radiant and convection heat transfer coefficients between the glass cover and ambient, respectively; T_{gla} , T_{a} , and T_{sky} are the temperatures of the glass cover, ambient, and sky, respectively.

The thermal equilibrium equation for the absorber plate is:

$$\tau_{\text{gla}} \alpha_{\text{abs}} I = h_{\text{r,abs-gla}} (T_{\text{abs}} - T_{\text{gla}}) + h_{\text{r,abs-b}} (T_{\text{abs}} - T_{\text{b}}) + h_{\text{cond,abs-tb}} (T_{\text{abs}} - T_{\text{tb}}) \quad (8)$$

with,

$$h_{\text{r,abs-b}} = \frac{\sigma(T_{\text{abs}}^2 + T_{\text{b}}^2)(T_{\text{abs}} + T_{\text{b}})}{\frac{1}{\varepsilon_{\text{abs}}} + \frac{1}{\varepsilon_{\text{b}}} - 1} \quad (9)$$

$$h_{\text{cond,abs-tb}} = \frac{\lambda_{\text{weld}} b}{f} \quad (10)$$

where, $h_{\text{r,abs-b}}$ is the radiant heat transfer coefficient between the absorber plate and bottom plate; $h_{\text{cond,abs-tb}}$ is the conductivity heat transfer coefficient between the absorber plate and absorber tubes; ε_{b} is the emissivity of the bottom plate; λ_{weld} , b , and f are the thermal conductivity coefficient, average width and average thickness of the welding material, respectively; and T_{abs} , T_{tb} , and T_{b} are the temperatures of the absorber plate, absorber tube, and bottom plate, respectively.

The thermal equilibrium equation for the absorber tube is [45]:

$$h_{\text{cond,abs-tb}} (T_{\text{abs}} - T_{\text{tb}}) = h_{\text{tb-f}} (T_{\text{tb}} - T_{\text{f}}) \quad (11)$$

with,

$$h_{\text{tb-f}} = (1430 + 23.3T_{\text{f}} - 0.048T_{\text{f}}^2)v_{\text{f}}^{0.8} D_{\text{in}}^{-0.2} \quad (12)$$

where, $h_{\text{tb-f}}$ is the heat transfer coefficient between the absorber tubes and the HTF; and T_{f} is the fluid temperature that is considered constant during the phase change process.

The temperature of the heat transfer fluid will rise by absorbing the heat from absorber tubes:

$$h_{\text{tb-f}} (T_{\text{tb}} - T_{\text{f}}) = c_p m (T_{\text{out}} - T_{\text{in}}) \quad (13)$$

where, T_{out} and T_{in} are the temperatures of the outlet and inlet HTF, respectively.

The thermal equilibrium equation for the back plate is:

$$h_{r,abs-b}(T_{abs} - T_b) = h_{r,b-grd}(T_b - T_{grd}) + h_{c,b-a}(T_b - T_a) \quad (14)$$

with,

$$h_{r,b-grd} = \frac{\sigma(T_b^2 + T_{grd}^2)(T_b + T_{grd})}{\frac{1}{\varepsilon_{grd}} + \frac{1}{\varepsilon_b} - 1} \quad (15)$$

$$h_{c,b-a} = 5.7 + 3.8v_{wind} \quad (16)$$

where, $h_{r,b-grd}$ is the radiant heat transfer coefficient between the bottom plate and ground; $h_{c,b-a}$ is the convection heat transfer coefficient for the bottom plate and the ambient surroundings.

Since each heat transfer coefficient for the above equations is closely related to the temperature of each component, the calculation process should be iterated until the accuracy of the results is satisfied. After the experiment and simulation calculation (as shown in Fig. 2), the mean relative error between them is 1.80%, implying that the model is reliable.

The second-stage solar field also utilizes the evacuated flat-plate solar collector for harvesting solar energy, but the working fluid of this stage is under the two-phase flow condition, i.e., the solar collector is under the direct steam generation working mode. The numerical model for the direct steam generation mode of the EFPC resembles that of the pressurized water mode, while the main distinction is the presence of two-phase flow in the absorber tubes. Hence, the subsequent model primarily focuses on estimating the boiling heat transfer coefficient, and the simulation steps are summarized in the flow chart (see Fig. 3).

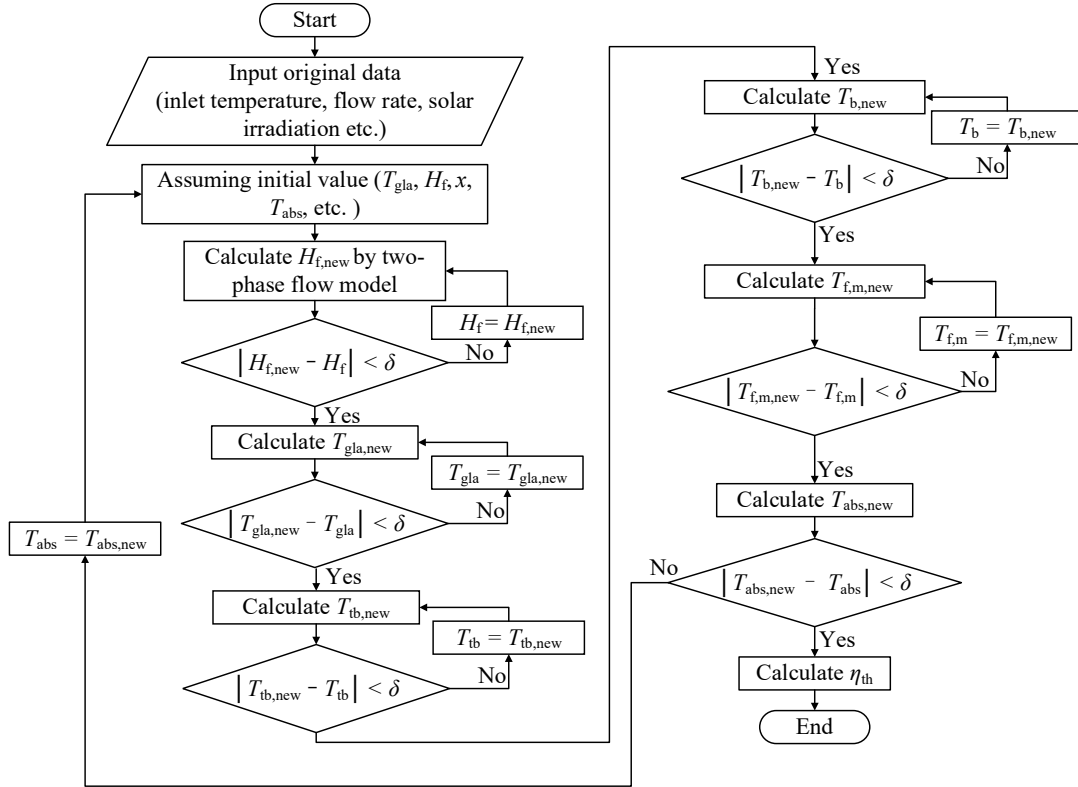


Fig. 3 Calculation flow chart of EFPC under the direct steam generation mode.

Through the correlation proposed by Gungor and Winterton [46], the two-phase flow heat transfer process is divided into two components: a nucleate boiling contribution and a single-phase convection contribution for saturated water.

$$h_{2p,f} = Sh_{nb} + Eh_1 \quad (17)$$

The factor S reflects the suppressed superheat amid forced convection compared with pool boiling, and it can be expressed as:

$$S = (1 + 1.15 \times 10^6 E^2 Re_l^{1.17})^{-1} \quad (18)$$

where, Re_l is the Renold number of the liquid phase:

$$Re_l = \frac{G(1-x)D_{in}}{\mu_l} \quad (19)$$

where, G is the mass flux, $kg/(m^2 \cdot s)$; x is the vapor quality, D_{in} is the inner diameter of the tube, m ; μ_l is the dynamic viscosity of the working fluid, $Pa \cdot s$.

Factor E represents the enhanced convection and higher velocity in the two-phase flow compared with the single-phase flow condition.

$$E = 1 + 24000Bo^{1.16} + 1.37Xtt^{-0.86} \quad (20)$$

where, Bo and Xtt are two dimensionless numbers that are called the boiling number and Martinelli number, respectively. They are expressed as:

$$Bo = \frac{q_{abs}}{G \cdot r} \quad (21)$$

$$Xtt = \left(\frac{\rho_g}{\rho_l} \right)^{0.5} \left(\frac{\mu_l}{\mu_g} \right)^{0.1} \left(\frac{1-x}{x} \right)^{0.9} \quad (22)$$

where, q_{abs} is the thermal flux, W/m^2 ; r is the phase change latent heat, J/kg ; and ρ_g and ρ_l are the density of the liquid and vapor phases, respectively, kg/m^3 . The physical property parameters are calculated at the saturated state by REFPROP 10.0 software.

The nucleate boiling coefficient h_{nb} can be calculated as:

$$h_{nb} = 55p_r^{0.12} (-\log_{10} p_r)^{-0.35} M^{-0.5} q_{abs}^{0.67} \quad (23)$$

where, p_r is the ratio between the pressure in the flow tube and the critical pressure of the working fluid. M is the relative molecular mass of the working fluid, g/mol .

The single-phase forced convection flow in the tube is modeled with the Dittus-Boelter equation [47]:

$$h_1 = 0.023 \left(\frac{\lambda_1}{D_{in}} \right) Re_1^{0.8} Pr_1^{0.4} \quad (24)$$

where, λ is the thermal conductivity, $W/(m \cdot K)$, and Pr is the Prandtl number.

The pressure drop of the two-phase flow is sourced from the actual data of solar steam collectors [48]. For a two-phase flow, the pressure drop is defined as the product of the single-phase water flow and factor R .

$$\left(\frac{dp}{dl}\right)_{2p} = R \left(\frac{dp}{dl}\right)_1 \quad (25)$$

with,

$$\left(\frac{dp}{dl}\right)_1 = 0.316 \text{Re}^{-0.25} \frac{1}{D_{\text{in}}} \frac{\rho}{2} v^2 \quad (26)$$

$$R = A + 3.43x^{0.685} (1-x)^{0.24} \left(\frac{\rho_l}{\rho_g}\right)^{0.5} \left(\frac{\mu_g}{\mu_l}\right)^{0.22} \left(1 - \frac{\mu_g}{\mu_l}\right)^{0.89} Fr_l^{-0.47} We_l^{0.0334} \quad (27)$$

where, $(dp/dl)_l$ is the pressure drop of the single-phase flow. ρ and v are the liquid density and velocity, respectively. The parameters for factor R are expressed as follows:

$$A = (1-x)^2 + x^2 \left(\frac{\rho_l}{\rho_g} \cdot \frac{\xi_g}{\xi_l}\right)^{0.8} \quad (28)$$

$$Fr_l = \frac{G^2}{\rho^2 g D_{\text{in}}} \quad (29)$$

$$We_l = \frac{G^2 D_{\text{in}}}{\rho \gamma} \quad (30)$$

where, g is the gravitational acceleration, m/s^2 , and γ is the surface tension, N/m .

By the above two-phase flow model, $h_{2p,f}$ can be obtained and Eq. (13) will be:

$$h_{\text{cond,abs-tb}} (T_{\text{abs}} - T_{\text{tb}}) = h_{\text{tb-f}} (T_{\text{tb}} - T_{\text{f}}) \quad (31)$$

with,

$$h_{\text{tb-f}} = \left(\ln \left(\frac{D_{\text{out}}}{D_{\text{in}}} \right) \left[\frac{1}{2\pi\lambda_{\text{tb}} l_{\text{tb}}} + \frac{1}{h_{2p,f}} \right] \right)^{-1} \quad (32)$$

where, $h_{\text{tb-f}}$ is the heat transfer coefficient between absorber tubes and the HTF, which comprises the heat conductivity of the absorber tube itself and the two-phase flow boiling heat transfer coefficient of the HTF; D_{out} , D_{in} , λ_{tb} , and l_{tb} are the inner and outer diameters, thermal conductivity, and length of the absorber tubes, respectively; and $h_{2p,f}$ is the two-phase heat transfer coefficient of the working fluid, which can be calculated

from the above numerical model.

To validate the numerical model of the second-stage solar field, as depicted in Fig. 4, the heat transfer coefficient is measured with respect to the different outlet steam qualities to indicate the key energy transfer process (i.e., two-phase flow heat transfer) of the second-stage solar field. The mean relative error between the experiment and simulation is 1.81%, which also leads to acceptable model accuracy.

The results of the author's previous work [40] have indicated that the thermal efficiency can be tremendously enhanced in the direct steam generation mode owing to the lower average operating temperature of the solar plant. In the intermediate temperature range, the solar thermal efficiency increment is approximately 10% higher (absolute value) than the pressurized water mode. Moreover, the outlet steam quality can be adjusted by the pump to avoid the influence of the varying solar irradiance during the day, which guarantees steady operation both in the solar plant and the ORC unit in this study.

According to the operation strategy, the system's running parameters will be manipulated by the boundary conditions, such as the HTF flow rate. For the two-stage solar field, the variable HTF flow rate has different impacts on them. The higher flow rate on the first stage solar field will degrade the average operating temperature, thus improving the solar harvesting efficiency to some degree. However, the higher flow rate on the second-stage solar field will reduce the outlet steam quality, thereby reducing the two-phase heat transfer coefficient and cutting down the solar harvesting efficiency to some degree. For brevity, we have taken account into the constantly

changing boundary conditions in this study and established the thermal model with steady energy harvesting processes in each time step.

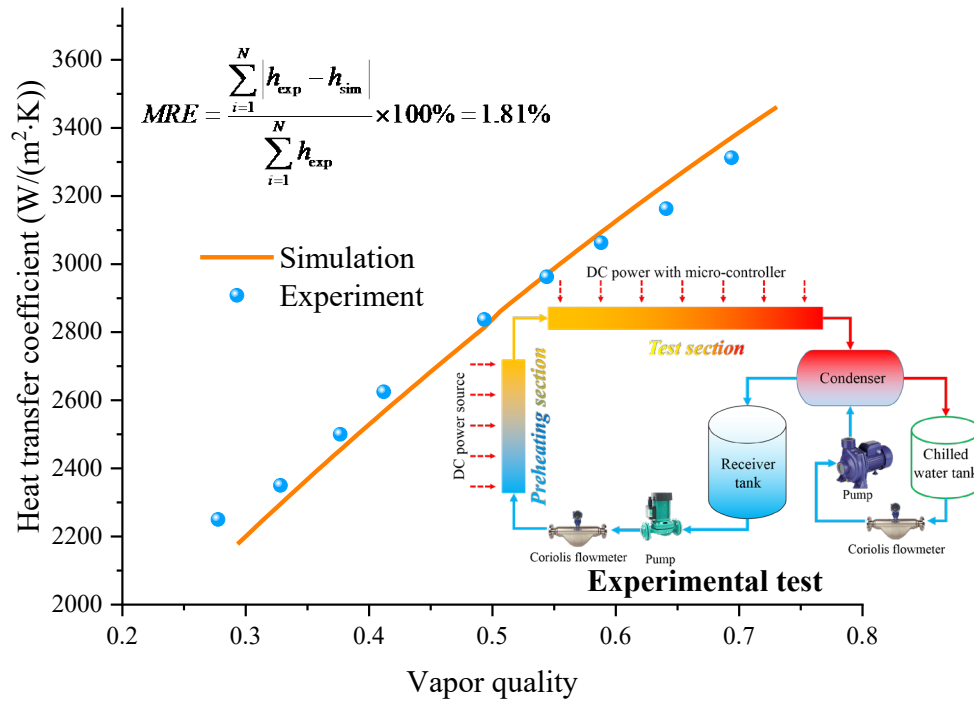


Fig. 4 Experimental validation of the second-stage solar field.

3.2 High-temperature accumulator

The HTA is a key component in transmitting energy from the solar plant to the ORC unit and is designed to effectively mitigate the effects of solar irradiation. It is assumed that the steam and water in the accumulator are in the equilibrium state. As presented in Fig. 5, the mass and energy exchange of the accumulator is divided into the water phase and steam phase, which is essential for modeling the process.

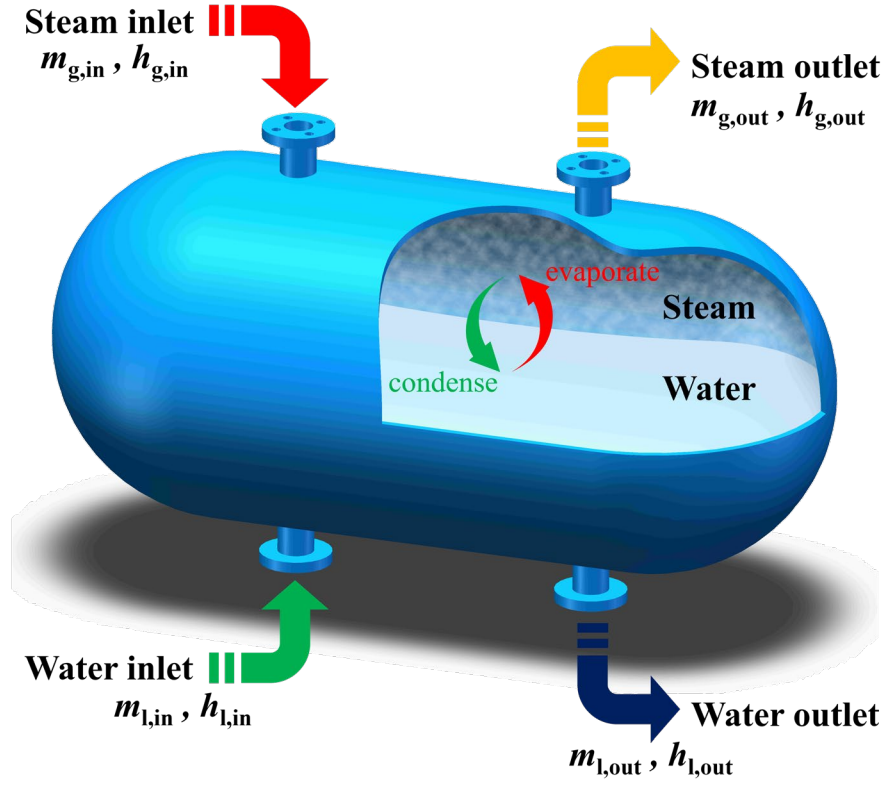


Fig. 5 Mass and energy flow of the HTA.

During the operation of the accumulator, the mass conservation equation is formulated as:

$$\frac{dM}{dt} = m_{l,in} - m_{l,out} + m_{g,in} - m_{g,out} \quad (33)$$

where, M refers to the mass of the HTF in the accumulator, kg; t is the time, s; and m is the mass flow rate, kg/s.

During the operation of the accumulator, the energy conservation equation is formulated as [49]:

$$\begin{aligned} \frac{dH}{dt} = & m_{l,in} h_{l,in} - m_{l,out} h_{l,out} + m_{g,in} h_{g,in} \\ & - m_{g,out} h_{g,out} + V \frac{dp}{dt} \end{aligned} \quad (34)$$

where, H denotes the total enthalpy in the HTA, J; h is the specific enthalpy, J/kg; V refers to the volume of the HTA, m³; and p is the pressure in the HTA, Pa.

Since $H = Mh$, Eq. (34) can be written as:

$$\frac{dH}{dt} = M \frac{dh}{dt} + h \frac{dM}{dt} \quad (35)$$

The specific enthalpy of the water and steam in the HTA is calculated as $h = h' + xr$. The quality is predicted as $x = (v - v') / (v'' - v')$. The specific enthalpy derivative is:

$$\frac{dh}{dt} = \left(\frac{dh'}{dp} + x \frac{dr}{dp} \right) \frac{dp}{dt} + r \frac{dx}{dt} \quad (36)$$

where, x is the quality of the steam in the HTA; r is the latent heat of water, J/kg; and h' refers to the specific enthalpy at the saturated water condition, J/kg.

Based on the above equations, the dynamic behavior (including T , p , H , x , etc.) of the HTA can be obtained.

3.3 The ORC unit

The numerical model of the ORC is established in this section. R245fa (critical pressure: 3.651 MPa, critical temperature: 427.16 K, ODP: 0, GWP: 1030 [50]) is used as the working fluid in the ORC unit. The main design parameters are summarized in Table 2.

Table 2 The main design parameters of the ORC unit.

Item	Value
ORC design power/(kW)	3.5
Expander's isentropic efficiency [51]	0.85
Generator's efficiency [35]	0.95
Pump's efficiency [52]	0.85
Heat exchanger pinch point/(K) [53]	5
Design solar irradiance/(W/m ²)	800
Working fluid of ORC unit	R245fa

The organic vapor expands to drive the turbine and generator; hence, the work produced by the screw turbine is [35]:

$$\begin{aligned} w_{\text{tur}} &= m_{\text{ORC}}(h_{\text{tur,in}} - h_{\text{tur,out}}) \\ &= m_{\text{ORC}}(h_{\text{tur,in}} - h_{\text{tur,out,s}})\eta_{\text{tur}} \end{aligned} \quad (37)$$

where, w_{tur} refers to the shaft power output of the turbine, W; m_{ORC} is the mass flow rate of organic fluid, kg/s; $h_{\text{tur,in}}$ is the inlet enthalpy of the turbine, J/kg; $h_{\text{tur,out}}$ is the outlet enthalpy of the turbine, J/kg; $h_{\text{tur,out,s}}$ is the isentropic outlet enthalpy of the turbine, J/kg; and η_{tur} is the adiabatic efficiency of the turbine.

The power produced by the generator is:

$$w_{\text{gen}} = w_{\text{tur}}\eta_{\text{gen}} \quad (38)$$

where, w_{gen} denotes the power generation of the generator, W; and η_{gen} is the efficiency of the generator.

The power consumed by the pump in the ORC is [54]:

$$\begin{aligned} w_{\text{p}} &= m_{\text{ORC}}(h_{\text{p,out}} - h_{\text{p,in}}) \\ &= m_{\text{ORC}}(h_{\text{p,out,s}} - h_{\text{p,in}})/\eta_{\text{p}} \end{aligned} \quad (39)$$

where, w_{p} refers to the power consumption of the pump, W; $h_{\text{p,in}}$ is the inlet enthalpy of the pump, J/kg; $h_{\text{p,out}}$ is the outlet enthalpy of the pump, J/kg; $h_{\text{p,out,s}}$ is the isentropic outlet enthalpy of the pump, J/kg; and η_{p} is the adiabatic efficiency of the pump.

The thermal to power of the ORC unit and the overall system solar-power conversion efficiencies are calculated by [50]:

$$\eta_{\text{ORC,th-pow}} = \frac{w_{\text{gen}} - w_{\text{p}}}{m_{\text{ORC}}(h_{\text{eva,out}} - h_{\text{eva,in}})} \quad (40)$$

where, $\eta_{\text{ORC,th-pow}}$ is the efficiency of thermal energy to power; $h_{\text{eva,in}}$ is the inlet enthalpy of the evaporator, J/kg; and $h_{\text{eva,out}}$ is the outlet enthalpy of the evaporator, J/kg.

and,

$$\eta_{\text{ORC,sol-pow}} = \frac{W_{\text{gen}} - W_{\text{p}}}{IA_{\text{SF}}} \quad (41)$$

where, $\eta_{\text{ORC,sol-pow}}$ is the efficiency of solar energy to power; I is the solar irradiance, W/m^2 ; and A_{SF} is the solar field area, m^2 .

4. Results and discussion

In this section, the thermodynamic behavior of the two-stage solar ORC system proposed in this paper is presented, including the solar harvesting performance, the power generation performance, and so forth. Moreover, a comparison with the traditional single-stage solar ORC system is also conducted.

4.1 Operation temperature optimization

The operation temperature of the solar plant is crucial to the entire system. It is not only closely related to the efficiency of the first- and second-stage solar plants but also has an immense impact on the operation of the ORC unit. The higher temperature will diminish the solar collector's efficiency but improve the thermal efficiency of the ORC unit, and vice versa. Hence, operation temperature optimization is conducted to strike a balance between these two processes. The outcomes are established under steady-state conditions.

The efficiencies of the solar plant, ORC unit, and the overall system are shown in Fig. 6. With the operating temperature rising, the efficiency of the two-stage solar plant decreases due to the progressive heat loss to the environment. However, the ORC unit power output will increase due to the higher evaporation temperature. The system's

efficiency as defined by Eq. (41) will be influenced by the above two energy conversion processes. Therefore, it is noticed that there exists an optimum operating temperature owing to the reasons mentioned before. In consideration of the thermal performance of the solar plant and the ORC unit, this temperature is designated as the operating temperature of the whole two-stage solar-driven ORC system.

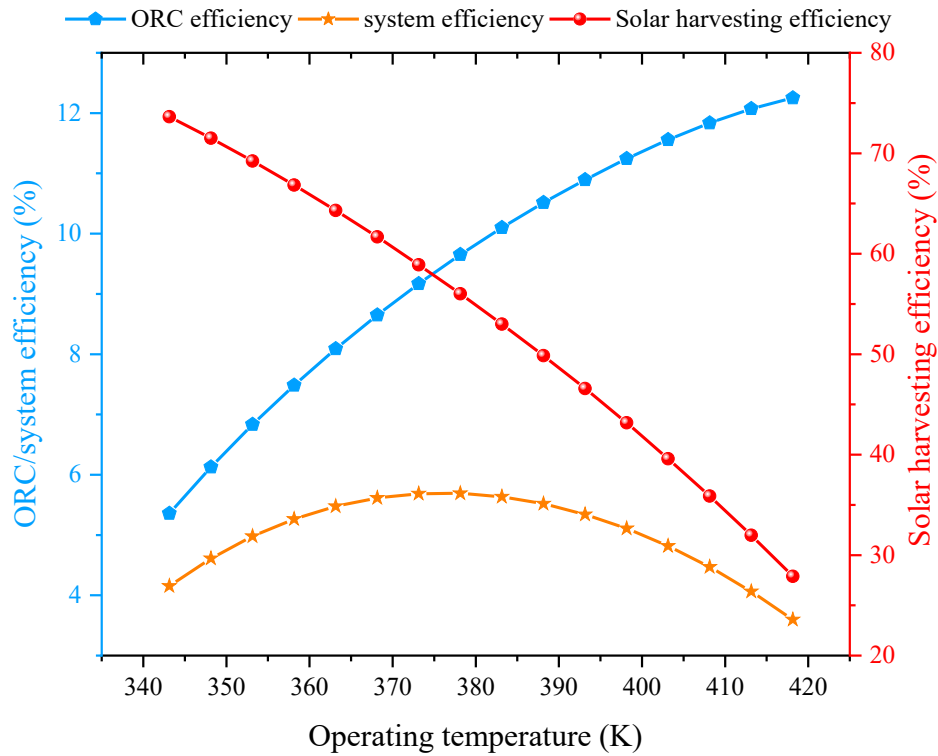
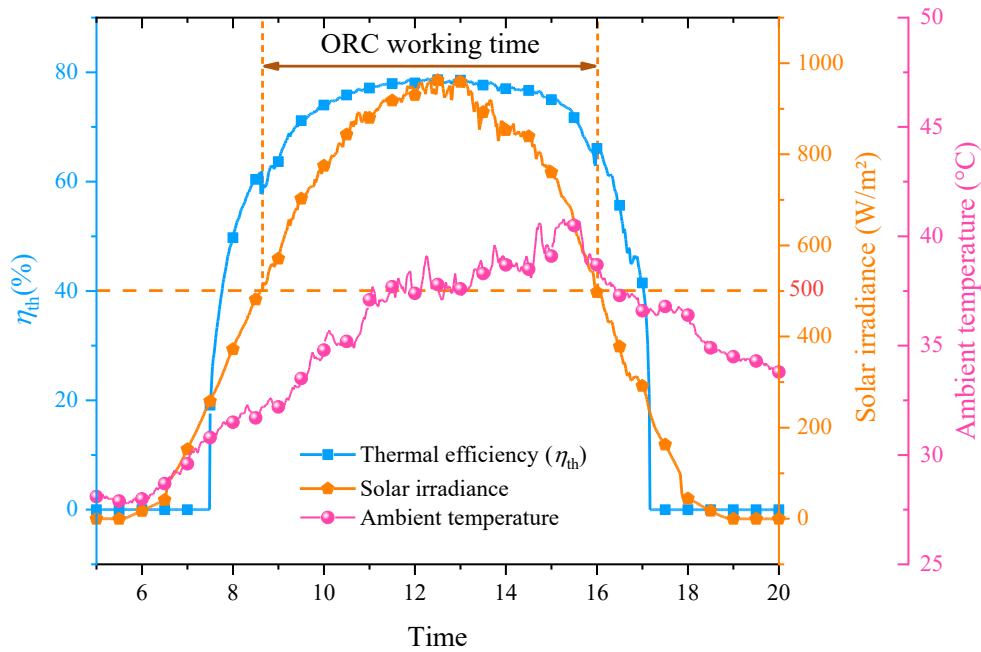


Fig. 6 Optimization of the system operating temperature.

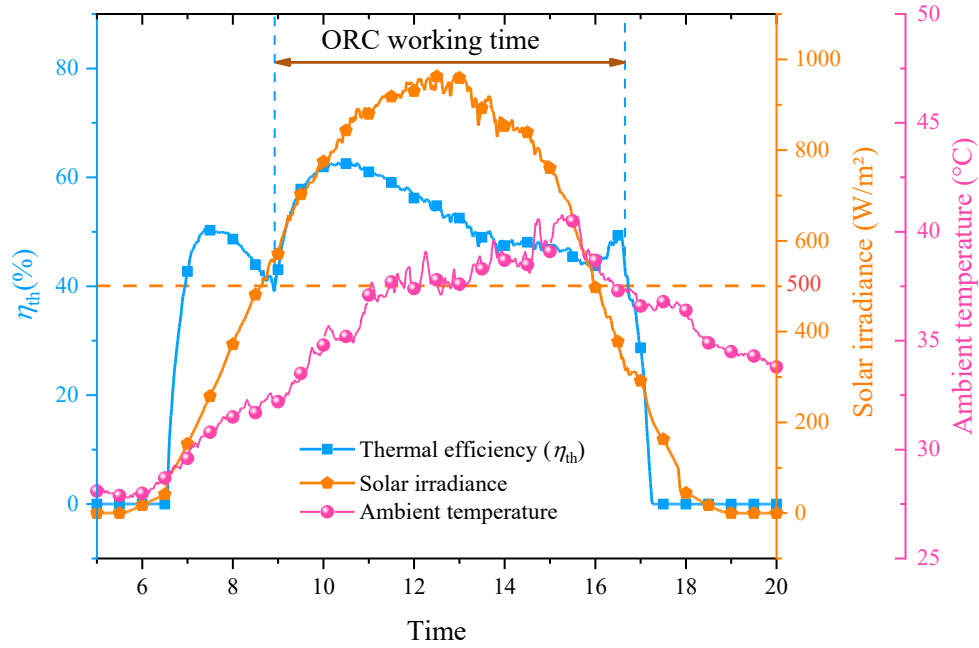
4.2 Solar thermal collection performance comparison

A typical sunny day is chosen in Hefei, China, and the solar irradiance, ambient temperature, and wind speed are recorded as the boundary conditions for the system operation. The two-stage solar-driven system runs throughout the in compliance with the aforementioned running strategies. Under the circumstance of systemic optimum working conditions, the real-time solar efficiency is depicted in Fig. 7 (a). For comparison purposes, the traditional solar ORC system, i.e., single-stage solar thermal

collection and heat accumulator storage, is also modeled and presented in Fig. 7 (b). In the single-stage solar-ORC working scheme, the ORC unit will start when the temperature of the storage accumulator reaches its design value and stop when the solar irradiance is weak and the temperature of the storage accumulator cannot provide enough thermal energy for the ORC unit [55]. The other system component type, such as the solar collector and ORC unit configuration (working fluid, efficiency parameters, etc.) are kept the same.



(a)



(b)

Fig. 7 Solar field efficiency during the day: (a) two-stage solar ORC system and (b) traditional single-stage solar ORC system.

In the case of the two-stage solar thermal collection scenario, the solar thermal efficiency is steadier in mode II due to the two-phase flow in the solar plant. It is observed that the solar harvesting efficiency exceeded 60% under abundant solar irradiance conditions. Whereas in the single-stage solar plant, the solar thermal efficiency immensely relies on the ambient and ORC working conditions. Initially, the solar thermal efficiency decreases since the temperature of the heat accumulator increases. With the initiation of the ORC unit, the stored thermal energy will be consumed and the decreasing temperature leads to higher solar thermal efficiency. However, with the assistance of a two-stage solar thermal collection plant and the operating strategy of the whole system, this fluctuation will be relieved by the relatively stable operation temperature in the solar plant. Thus, it is proven that the system configuration of this paper can bring benefits to the solar thermal collection process.

4.3 Thermodynamic behavior of the HTA

The enthalpy variation of the HTA is shown in Fig. 8. Its upward trend aligns with the solar irradiance but reaches the maximum value at different moments. This discrepancy can be ascribed to the systematic design strategies: When the solar irradiance reaches its peak value at noon, the energy gained by the solar plant will exceed the energy requirement of the ORC unit. Hence, the enthalpy in the HTA will keep increasing owing to the energy storage capacity of the HTA. When the solar irradiance is lower than the threshold value as the strategies designed, the enthalpy will start to decrease since the solar energy gain is insufficient to meet the energy requirement of the ORC unit. This observation aligns with the initial principles governing the system design.

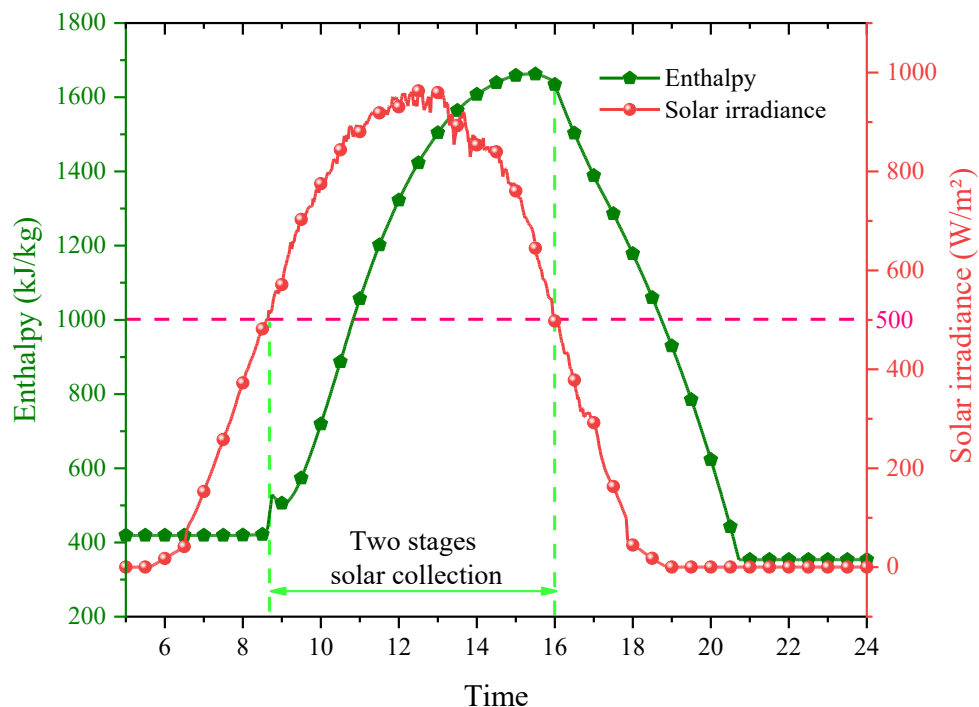
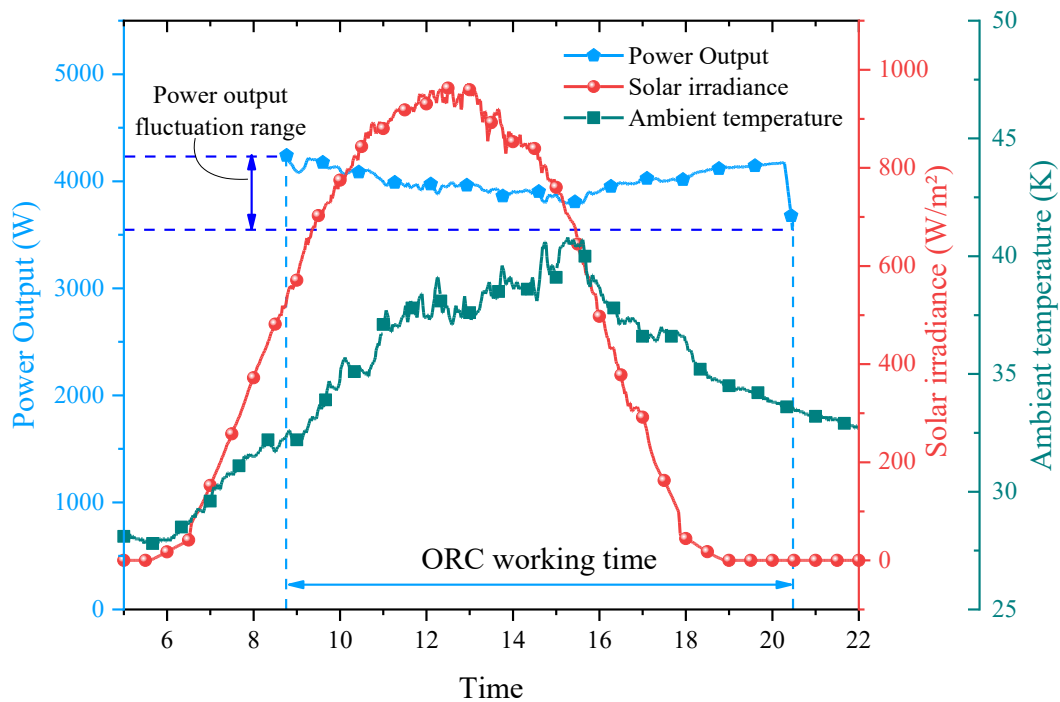


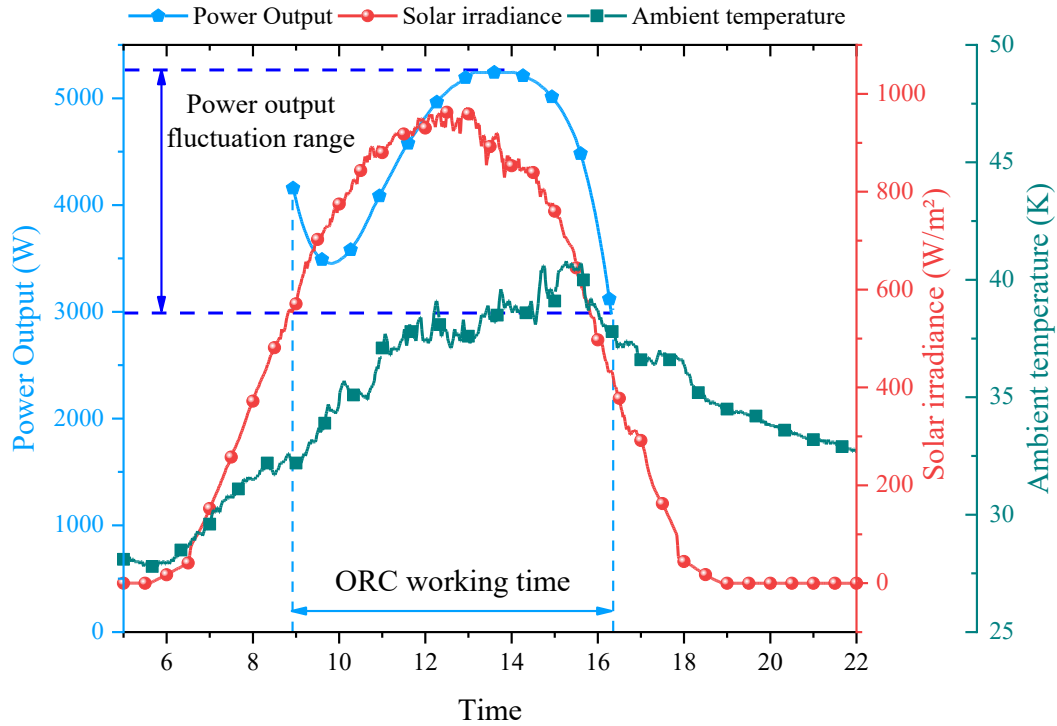
Fig. 8 The enthalpy variation during the day.

4.4 Power generation performance comparison

The primary objective of the two-stage solar ORC system design in this study is to reduce the impact of solar irradiation on the ORC power output. To prove the actual effect of this design, the final power generation by the ORC unit is presented in Fig. 9, showcasing a relatively narrow range of variation in power output once the solar irradiance reaches a certain threshold (after 9:00). The electricity output power ranges from approximately 3500 W to 4200 W throughout the day. The variability in power can be attributed to changes in ambient temperature, which directly affect the performance of the condenser in the ORC unit. Hence, it is proven that this system configuration and strategy design can eliminate the influence of solar irradiance fluctuation and benefit ORC operation. On average, the overall system efficiency of the two-stage system is 6.43% over the daytime.



(a)



(b)

Fig. 9 The power generation of the (a) two-stage solar ORC system and (b) conventional single-stage solar ORC system.

Under the same configuration (solar field area, the capacity of the storage accumulator, etc.) of this two-stage system deployment, the power output situation of the conventional solar ORC system is also presented in Fig. 9 (b). This single-stage solar ORC system adopted a stratification storage tank for energy delivery from the solar field to the ORC unit. The numerical model of the stratification storage tank has been widely used in previous studies and proved to be a satisfactory result [56]. It can be observed that the output power is closely related to the solar irradiance magnitude after the temperature in the storage accumulator has reached the setting point. The drop at the beginning (around 10:00 a.m.) is attributed to limited energy stored in the morning, and the energy consumed by the ORC unit is higher than the solar energy collected during that period. The fluctuation in electricity output primarily stems from

the supply of energy from the solar field, which significantly affects the evaporation temperature of the ORC unit. During the daily working time, its power generation ranges from about 3000 W to 5300 W. Moreover, although the maximum output power has exceeded the two-stage system proposed in this paper, the effective working time during the whole day is much shorter (stop at around 16:00) than that of the two-stage system (stop at around 20:00). The reason can be ascribed to the lower solar thermal collection and overall system efficiency of the conventional system (4.47% over the daytime). Therefore, the well-designed system configuration can not only sustain a steady system running situation (the fluctuation range has been reduced by approximately 70%) but also improve the overall system efficiency by 43.85% during the typical day. In addition, the total power output of the two-stage system is 2925.48 kWh, while the single-stage system can only provide 2034.29 kWh during the whole day.

5. Conclusions

The off-design operation of the solar-driven Organic Rankine Cycle system has greatly impeded its widespread adoption in district energy systems. To tackle the solar irradiance fluctuation impact on the Organic Rankine Cycle unit off-design running problem, a novel solar-driven Organic Rankine Cycle system is proposed in this paper that incorporates the two-stage solar thermal collection and heat accumulation units. To realize the above design, a structure-optimized non-concentrating solar collector is adopted to produce steam for better solar thermal collection and Organic Rankine Cycle system operation. The dynamic models for the steam accumulator and Organic Rankine

Cycle unit are established to prove the system's feasibility and superiority. The main conclusions are drawn as follows.

- (1) The two-stage solar thermal collection design, featuring a novel non-concentrating solar collector, achieves high solar efficiency (average > 60%) during the day. In contrast, the solar thermal efficiency of a single-stage conventional solar Organic Rankine Cycle system is heavily reliant on the working condition of the system. Consequently, much more solar energy is captured and the steady heat source supply of the two-stage solar Organic Rankine Cycle system is guaranteed.
- (2) Profiting from the system design and operation strategy, the two-stage accumulation design can provide a steady heat source to the Organic Rankine Cycle unit running and avoid the off-design condition. It can bring benefits to both the solar Organic Rankine Cycle system running and users' demand. The power output fluctuation range has been reduced by approximately 70% via the two-stage solar Organic Rankine Cycle system. Therefore, the tremendous impact of the evaporation temperature (depending on the solar energy supply) on the Organic Rankine Cycle operation is mitigated.
- (3) With the proper system design in this paper, the running time of the solar Organic Rankine Cycle system can be prolonged. Under the same ambient conditions, the running time of the two-stage solar Organic Rankine Cycle system is 4 hours longer than that of the conventional system.
- (4) Based on the aforementioned analysis, the overall system efficiency is improved by 43.85% via the implementation of the two-stage system design, which promotes

the development of solar Organic Rankine Cycle technology and breaks new ground.

This study provides a new approach to the development of solar-driven ORC systems. A major challenge in implementing such a two-stage solar system lies in designing real-time controllers capable of monitoring parameter variations and instructing the system component to adjust its operation accordingly. Future research should focus on the tech-economic and environmental performance assessment of the system, as well as its practical applications.

Acknowledgments

The study was sponsored by the National Natural Science Foundation of China (NSFC 52130601). The authors are grateful for support from the Joint research center for multi-energy complementation and conversion of the University of Science and Technology of China.

References

- [1] Z.Y. Tian, B. Perers, S. Furbo, J.H. Fan, Annual measured and simulated thermal performance analysis of a hybrid solar district heating plant with flat plate collectors and parabolic trough collectors in series, *Applied Energy*, 205 (2017) 417-427. <https://doi.org/10.1016/j.apenergy.2017.07.139>
- [2] X.R. Wang, L. Xia, C. Bales, X.X. Zhang, B. Copertaro, S. Pan, J.S. Wu, A systematic review of recent air source heat pump (ASHP) systems assisted by solar thermal, photovoltaic and photovoltaic/thermal sources, *Renewable Energy*, 146 (2020) 2472-2487. <https://doi.org/10.1016/j.renene.2019.08.096>
- [3] M. Hosenuzzaman, N.A. Rahim, J. Selvaraj, M. Hasanuzzaman, A.B.M.A. Malek, A. Nahar, Global prospects, progress, policies, and environmental impact of solar photovoltaic power generation, *Renewable & Sustainable Energy Reviews*, 41 (2015) 284-297. <https://doi.org/10.1016/j.rser.2014.08.046>
- [4] U. Desideri, P.E. Campana, Analysis and comparison between a concentrating solar and a photovoltaic power plant, *Applied Energy*, 113 (2014) 422-433. <https://doi.org/10.1016/j.apenergy.2013.07.046>

- [5] L. Mauler, F. Duffner, W.G. Zeier, J. Leker, Battery cost forecasting: a review of methods and results with an outlook to 2050, *Energy & Environmental Science*, 14 (2021) 4712-4739. <https://doi.org/10.1039/d1ee01530c>
- [6] Renewable Power Generation Costs in 2020, in, International Renewable Energy Agency, Abu Dhabi.
- [7] O.B. Mousa, S. Kara, R.A. Taylor, Comparative energy and greenhouse gas assessment of industrial rooftop-integrated PV and solar thermal collectors, *Applied Energy*, 241 (2019) 113-123. <https://doi.org/10.1016/j.apenergy.2019.03.052>
- [8] Power Generation and Cumulative Capacity of Solar Thermal Power Plants in China (2017 – 2021), 2023, 25th, Jun., <https://www.globaldata.com/data-insights/power-and-utilities/power-generation-and-cumulative-capacity-of-solar-thermal-power-plants-in-china-2017-2021/#:~:text=The%20global%20installed%20solar%20thermal,reach%2014%2C172.8%20MW%20by%202030.>
- [9] E. Vengadesan, A.R.I. Rumaney, R. Mitra, S. Harichandan, R. Senthil, Heat transfer enhancement of a parabolic trough solar collector using a semicircular multitube absorber, *Renewable Energy*, 196 (2022) 111-124. <https://doi.org/10.1016/j.renene.2022.06.148>
- [10] J.L. Chen, G. Xiao, H.R. Xu, X. Zhou, J.M. Yang, M.J. Ni, K.F. Cen, Experiment and dynamic simulation of a solar tower collector system for power generation, *Renewable Energy*, 196 (2022) 946-958. <https://doi.org/10.1016/j.renene.2022.07.045>
- [11] P.C. Li, J. Li, G.T. Gao, G. Pei, Y.H. Su, J. Ji, B. Ye, Modeling and optimization of solar-powered cascade Rankine cycle system with respect to the characteristics of steam screw expander, *Renewable Energy*, 112 (2017) 398-412. <https://doi.org/10.1016/j.renene.2017.05.054>
- [12] T.Y. Xiao, C. Liu, X.R. Wang, S.K. Wang, X.X. Xu, Q.B. Li, X.X. Li, Life cycle assessment of the solar thermal power plant integrated with air-cooled supercritical CO₂ Brayton cycle, *Renewable Energy*, 182 (2022). <https://doi.org/10.1016/j.renene.2021.10.001>
- [13] John A. Duffie, W.A. Beckman, *Solar Engineering of Thermal Processes*, John Wiley & Sons, Inc., Hoboken, New Jersey, 2013.
- [14] M. Bezaatpour, H. Rostamzadeh, Design and evaluation of flat plate solar collector equipped with nanofluid, rotary tube, and magnetic field inducer in a cold region, *Renewable Energy*, 170 (2021) 574-586. <https://doi.org/10.1016/j.renene.2021.02.001>
- [15] O.A. Lopez-Nunez, J.A. Alfaro-Ayala, J.J. Ramirez-Minguela, F.C. Banda, B. Ruiz-Camacho, J.M. Belman-Flores, Numerical analysis of the thermo-hydraulic performance and entropy generation rate of a water-in-glass evacuated tube solar collector using TiO₂ water-based nanofluid and only water as working fluids, *Renewable Energy*, 197 (2022) 953-965. <https://doi.org/10.1016/j.renene.2022.07.156>
- [16] A. Naminezhad, M. Mehregan, Energy and exergy analyses of a hybrid system integrating solar-driven organic Rankine cycle, multi-effect distillation, and reverse osmosis desalination systems, *Renewable Energy*, 185 (2022) 888-903. <https://doi.org/10.1016/j.renene.2021.12.076>
- [17] L.B. Wang, X.B. Bu, H.S. Li, Multi-objective optimization and off-design evaluation of organic rankine cycle (ORC) for low-grade waste heat recovery, *Energy*, 203 (2020). <https://doi.org/10.1016/j.energy.2020.117809>
- [18] D. Gao, L. Wu, Y. Hao, G. Pei, Ultrahigh-efficiency solar energy harvesting via a non-concentrating evacuated aerogel flat-plate solar collector, *Renewable Energy*, 196 (2022) 1455-1468. <https://doi.org/10.1016/j.renene.2022.07.091>
- [19] A.A. Gunay, H. Kim, N. Nagarajan, M. Lopez, R. Kantharaj, A. Alsaati, A. Marconnet, A. Lenert, N. Miljkovic, Optically Transparent Thermally Insulating Silica Aerogels for Solar Thermal Insulation,

- Acs Applied Materials & Interfaces, 10 (2018) 12603-12611. <https://doi.org/10.1021/acsami.7b18856>
- [20] L. Zhao, B. Bhatia, S. Yang, E. Strobach, L.A. Weinstein, T.A. Cooper, G. Chen, E.N. Wang, Harnessing Heat Beyond 200 °C from Unconcentrated Sunlight with Nonevacuated Transparent Aerogels, *Acs Nano*, 13 (2019) 7508-7516. <https://doi.org/10.1021/acs.nano.9b02976>
- [21] M. Eltaweel, A.A. Abdel-Rehim, A.A.A. Attia, A comparison between flat-plate and evacuated tube solar collectors in terms of energy and exergy analysis by using nanofluid, *Applied Thermal Engineering*, 186 (2021). <https://doi.org/ARTN.116516>
10.1016/j.applthermaleng.2020.116516
- [22] Y. Shi, R.Y. Li, Y. Jin, S.F. Zhuo, L. Shi, J. Chang, S. Hong, K.C. Ng, P. Wang, A 3D Photothermal Structure toward Improved Energy Efficiency in Solar Steam Generation, *Joule*, 2 (2018) 1171-1186. <https://doi.org/10.1016/j.joule.2018.03.013>
- [23] H.Y. Ren, M. Tang, B.L. Guan, K.X. Wang, J.W. Yang, F.F. Wang, M.Z. Wang, J.Y. Shan, Z.L. Chen, D. Wei, H.L. Peng, Z.F. Liu, Hierarchical Graphene Foam for Efficient Omnidirectional Solar-Thermal Energy Conversion, *Advanced Materials*, 29 (2017). <https://doi.org/ARTN.1702590>
10.1002/adma.201702590
- [24] C. Kutlu, J. Li, Y. Su, G. Pei, S. Riffat, Off-design performance modelling of a solar organic Rankine cycle integrated with pressurized hot water storage unit for community level application, *Energy Conversion and Management*, 166 (2018) 132-145. <https://doi.org/10.1016/j.enconman.2018.04.024>
- [25] M.A. Chatzopoulou, M. Simpson, P. Sapin, C.N. Markides, Off-design optimisation of organic Rankine cycle (ORC) engines with piston expanders for medium-scale combined heat and power applications, *Applied Energy*, 238 (2019) 1211-1236. <https://doi.org/10.1016/j.apenergy.2018.12.086>
- [26] D. Hu, Y. Zheng, Y. Wu, S. Li, Y. Dai, Off-design performance comparison of an organic Rankine cycle under different control strategies, *Applied Energy*, 156 (2015) 268-279. <https://doi.org/https://doi.org/10.1016/j.apenergy.2015.07.029>
- [27] M. Weitzer, D. Müller, J. Karl, Two-phase expansion processes in heat pump – ORC systems (Carnot batteries) with volumetric machines for enhanced off-design efficiency, *Renewable Energy*, 199 (2022) 720-732. <https://doi.org/https://doi.org/10.1016/j.renene.2022.08.143>
- [28] R. Prasad, M. Ali, Y. Xiang, H. Khan, A double decomposition-based modelling approach to forecast weekly solar radiation, *Renewable Energy*, 152 (2020) 9-22. <https://doi.org/10.1016/j.renene.2020.01.005>
- [29] Y.Q. Feng, T.C. Hung, T.Y. Su, S. Wang, Q. Wang, S.C. Yang, J.R. Lin, C.H. Lin, Experimental investigation of a R245fa-based organic Rankine cycle adapting two operation strategies: Stand alone and grid connect, *Energy*, 141 (2017) 1239-1253. <https://doi.org/10.1016/j.energy.2017.09.119>
- [30] E.S. ELSihy, X.H. Wang, C. Xu, X.Z. Du, Numerical investigation on simultaneous charging and discharging process of molten-salt packed-bed thermocline storage tank employing in CSP plants, *Renewable Energy*, 172 (2021) 1417-1432. <https://doi.org/10.1016/j.renene.2020.11.139>
- [31] Q. Li, X.Q. Huang, Y.H. Tai, W.F. Gao, L. Wenxian, W.M. Liu, Thermal stratification in a solar hot water storage tank with mantle heat exchanger, *Renewable Energy*, 173 (2021) 1-11. <https://doi.org/10.1016/j.renene.2021.03.105>
- [32] A.G. Fernandez, J. Gomez-Vidal, E. Oro, A. Kruiženga, A. Sole, L.F. Cabeza, Mainstreaming commercial CSP systems: A technology review, *Renewable Energy*, 140 (2019) 152-176. <https://doi.org/10.1016/j.renene.2019.03.049>
- [33] J. Freeman, K. Hellgardt, C.N. Markides, Working fluid selection and electrical performance optimisation of a domestic solar-ORC combined heat and power system for year-round operation in the

- UK, *Applied Energy*, 186 (2017) 291-303. <https://doi.org/10.1016/j.apenergy.2016.04.041>
- [34] D.T. Gao, B. Zhao, T.H. Kwan, Y. Hao, G. Pei, The spatial and temporal mismatch phenomenon in solar space heating applications: status and solutions, *Applied Energy*, 321 (2022). <https://doi.org/10.1016/j.apenergy.2022.119326>
- [35] J. Li, G. Gao, C. Kutlu, K. Liu, G. Pei, Y. Su, J. Ji, S. Riffat, A novel approach to thermal storage of direct steam generation solar power systems through two-step heat discharge, *Applied Energy*, 236 (2019) 81-100. <https://doi.org/10.1016/j.apenergy.2018.11.084>
- [36] Y.L. He, K. Wang, Y. Qiu, B.C. Du, Q. Liang, S. Du, Review of the solar flux distribution in concentrated solar power: Non-uniform features, challenges, and solutions, *Applied Thermal Engineering*, 149 (2019) 448-474. <https://doi.org/10.1016/j.applthermaleng.2018.12.006>
- [37] G. Gao, J. Li, P. Li, H. Yang, G. Pei, J. Ji, Design and analysis of an innovative concentrated solar power system using cascade organic Rankine cycle and two-tank water/steam storage, *Energy Conversion and Management*, 237 (2021) 114108. <https://doi.org/https://doi.org/10.1016/j.enconman.2021.114108>
- [38] Q. Wang, J. Wang, T. Li, N. Meng, Techno-economic performance of two-stage series evaporation organic Rankine cycle with dual-level heat sources, *Applied Thermal Engineering*, 171 (2020) 115078. <https://doi.org/https://doi.org/10.1016/j.applthermaleng.2020.115078>
- [39] A. Surendran, S. Seshadri, Performance investigation of two stage Organic Rankine Cycle (ORC) architectures using induction turbine layouts in dual source waste heat recovery, *Energy Conversion and Management: X*, 6 (2020) 100029. <https://doi.org/https://doi.org/10.1016/j.ecmx.2020.100029>
- [40] D. Gao, J. Li, X. Ren, T. Hu, G. Pei, A novel direct steam generation system based on the high-vacuum insulated flat plate solar collector, *Renewable Energy*, 197 (2022) 966-977. <https://doi.org/10.1016/j.renene.2022.07.102>
- [41] W.D. Steinmann, M. Eck, Buffer storage for direct steam generation, *Solar Energy*, 80 (2006) 1277-1282. <https://doi.org/10.1016/j.solener.2005.05.013>
- [42] D. Gao, G. Gao, J. Cao, S. Zhong, X. Ren, Y.N. Dabwan, M. Hu, D. Jiao, T.H. Kwan, G. Pei, Experimental and numerical analysis of an efficiently optimized evacuated flat plate solar collector under medium temperature, *Applied Energy*, 269 (2020) 115129. <https://doi.org/10.1016/j.apenergy.2020.115129>
- [43] S.K. Verma, A.K. Tiwari, D.S. Chauhan, Experimental evaluation of flat plate solar collector using nanofluids, *Energy Conversion and Management*, 134 (2017) 103-115. <https://doi.org/10.1016/j.enconman.2016.12.037>
- [44] X. Ren, J. Li, M. Hu, G. Pei, D. Jiao, X. Zhao, J. Ji, Feasibility of an innovative amorphous silicon photovoltaic/thermal system for medium temperature applications, *Applied Energy*, 252 (2019) 113427. <https://doi.org/10.1016/j.apenergy.2019.113427>
- [45] V. Badescu, Optimum fin geometry in flat plate solar collector systems, *Energy Conversion and Management*, 47 (2006) 2397-2413. <https://doi.org/10.1016/j.enconman.2005.11.006>
- [46] K.E. Gungor, R.H.S. Winterton, A General Correlation for Flow Boiling in Tubes and Annuli, *International Journal of Heat and Mass Transfer*, 29 (1986) 351-358. [https://doi.org/10.1016/0017-9310\(86\)90205-X](https://doi.org/10.1016/0017-9310(86)90205-X)
- [47] S.K. Nellis Gregory, *Heat transfer*, Cambridge university press, 2008.
- [48] M. Eck, W.D. Steinmann, Modelling and design of direct solar steam generating collector fields, *Journal of Solar Energy Engineering-Transactions of the Asme*, 127 (2005) 371-380. <https://doi.org/10.1115/1.1849225>

- [49] V.D. Stevanovic, M.M. Petrovic, S. Milivojevic, B. Maslovaric, Prediction and Control of Steam Accumulation, Heat Transfer Engineering, 36 (2015) 498-510. <https://doi.org/10.1080/01457632.2014.935226>
- [50] S. Li, H.J. Ma, W.Y. Li, Dynamic performance analysis of solar organic Rankine cycle with thermal energy storage, Applied Thermal Engineering, 129 (2018) 155-164. <https://doi.org/10.1016/j.applthermaleng.2017.10.021>
- [51] W. Su, L. Zhao, S. Deng, W.C. Xu, Z.X. Yu, A limiting efficiency of subcritical Organic Rankine cycle under the constraint of working fluids, Energy, 143 (2018) 458-466. <https://doi.org/10.1016/j.energy.2017.11.003>
- [52] M.A. Ehyaei, A. Ahmadi, M.E. Assad, M.A. Rosen, Investigation of an integrated system combining an Organic Rankine Cycle and absorption chiller driven by geothermal energy: Energy, exergy, and economic analyses and optimization, Journal of Cleaner Production, 258 (2020). <https://doi.org/10.1016/j.jclepro.2020.120780>
- [53] A. Landelle, N. Tauveron, P. Haberschill, R. Revellin, S. Colasson, Organic Rankine cycle design and performance comparison based on experimental database, Applied Energy, 204 (2017) 1172-1187. <https://doi.org/10.1016/j.apenergy.2017.04.012>
- [54] D.K. Kim, J.S. Lee, J. Kim, M.S. Kim, M.S. Kim, Parametric study and performance evaluation of an organic Rankine cycle (ORC) system using low-grade heat at temperatures below 80 degrees C, Applied Energy, 189 (2017) 55-65. <https://doi.org/10.1016/j.apenergy.2016.12.026>
- [55] J. Freeman, K. Hellgardt, C.N. Markides, An assessment of solar-powered organic Rankine cycle systems for combined heating and power in UK domestic applications, Applied Energy, 138 (2015) 605-620. <https://doi.org/10.1016/j.apenergy.2014.10.035>
- [56] T.J. Bird, N. Jain, Dynamic modeling and validation of a micro-combined heat and power system with integrated thermal energy storage, Applied Energy, 271 (2020). <https://doi.org/10.1016/j.apenergy.2020.114955>